

# AN APPLICATION OF THE UNSCENTED KALMAN FILTER FOR SPACECRAFT ATTITUDE ESTIMATION ON REAL AND SIMULATED LIGHT CURVE DATA

**Kent A. Rush**

Author

M.S. Aerospace Engineering

California Polytechnic

San Luis Obispo

Email: kentalejandrорush@gmail.com

**Morgan Yost**

Co-author

Lockheed Martin Space

**Liam Smith**

Co-author

Lockheed Martin Space

**Andrew Zizzo**

Co-author

Lockheed Martin Space

*In the past, analyses of lightcurve data have been applied to asteroids in order to determine their axis of rotation, rotation rate and other parameters. In recent decades, these analyses have begun to be applied in the domain of Earth orbiting spacecraft. Due to the complex geometry of spacecraft and the wide variety of parameters that can influence the way in which they reflect light, these analyses require more complex assumptions and a greater knowledge about the object being studied. Previous investigations have shown success in extracting attitude parameters from unresolved spacecraft using simulated data. This paper presents a focused attempt to derive attitude parameters using an Unscented Kalman Filter from both simulated and real data provided by Lockheed Martin Space.*

*This paper characterizes and presents the differences in performance between three simulated geometries in low, medium, and geostationary orbit in both cases where they are spinning about a constant axis and in cases in which they are tumbling.*

*Additionally, this paper hypothesizes and tests the idea that a predictable and extraneous angular velocity solution exists which is the reflection of the true solution about the plane defined by the sun and observation vectors. This pa-*

*per encountered multiple instances of this type solution appearing in simulation and provides an example as well as a visualization.*

*Finally, this paper demonstrates the ability to converge to a solution from real data although there were large discrepancies between the measurement model and the data. This paper discusses the validity of these solutions and sources of error.*

## 1 Introduction

Light curve data is possible one of the most accessible and plentiful sources of data that can be acquired from a spacecraft. It requires nothing from the spacecraft and can be collected by anyone for as many passes as could be desired. Given that interest in utilizing Earth orbit has never been higher, the utility of this rich vein of data has also never been higher.

Because the light reflected from a spacecraft is so dependent on that spacecrafts geometry, attitude and material properties that it is possible to estimate these quantities. This paper focuses on the latter, but substantial work has already been published on the topic of geometry estimation.

Being able to estimate the attitude of a spacecraft for the duration of a pass also enables the estimation of its angular velocity, and these two quantities combined offer incredible potential to increase the situational awareness of space operations. For example, recently a well funded effort to deorbit space debris has begun both by government and commercial organizations. This undertaking must contend with the challenge that their targets are often spinning and telemetry is unavailable. Here, light curve data enables the spin of the target to be estimated without requiring telemetry and allows for operators to be prepared before proximity operations with the target begin.

Additionally, it offers a method of identifying and classifying uncatalogued objects. Because attitude and spin are so closely linked to the mission of a spacecraft, estimating these from light curve data allows for debris to be differentiated from functioning spacecraft and more.

In this paper, an Unscented Kalman Filter is formulated and tested against simulated data to verify proof of concept and characterize performance with respect to varying orbits and geometries. Additionally, a hypothesis is tested where a set of solutions which are indistinguishable from the truth exist but which is predictably related to the truth by the direction of illumination and observation.

Finally, this paper attempts to bring the theoretical prospects of lightcurve data into practical ones. Using high quality data provided by Lockheed Martin Space's Santa Cruz observation site, attitude and spin rate estimation will be attempted using real data and high fidelity geometric models of real spacecraft.

## 2 Unscented Kalman Filter Formulation

This paper actually utilizes two formulations of the UKF. The first formulation is derived for the case in which it can be assumed that the object is spinning about a fixed axis or is not tumbling. The second formulation is used in the case in which the object is expected to be tumbling or its axis of rotation is not constant.

### 2.1 Assumptions

This paper assumes knowledge of the spacecraft geometry. This assumption is used by Wetterer et. al., Holzinger et. al, to name a few [1] [2]. Alternative analyses have made attempts to estimate the geometry but have assumed knowledge of angular velocity [3] [4] [5] [6].

This paper derives a UKF which requires data that could be plausibly acquired in an analysis of real data. Unfortunately, this problem requires either the geometry or the angular velocity to be known as one cannot be determined without the other. This paper assumes that the geometry is accessible, either from photographs, access to design drawings or other means.

This paper does not assume any prior knowledge of attitude, angular velocity, or inertia of the object. The first formulation described is for the case in which the inertia does not need to be known which occurs when the object is spin-

ning about its major axis. The second includes the inertia in the state estimate to enable attitude estimation in the case of a tumbling object.

### 2.2 Non-Tumbling Formulation

The definition of the state vector is composed of the modified Rodriguez parameters and angular velocity and is in the form:

$$\mathbf{x} = \begin{bmatrix} \mathbf{p} \\ \boldsymbol{\omega} \end{bmatrix}, \quad (1)$$

where  $\mathbf{p}$  are the Modified Rodriguez Parameters (MRPs) and  $\boldsymbol{\omega}$  is the angular velocity vector. This formulation is utilized in this paper to filter data for objects that are assumed to be spinning about a constant axis or whose inertial properties are known. In either of these cases inertial properties do not need to be estimated.

The Modified Rodriguez Parameters were selected as the attitude representation of choice for this paper. The use of quaternions and Euler Angles were investigated but were not used for various reasons. Quaternions suffer from the issue that they are redundant (They constitute of four elements rather than the minimum of three) and are constrained to unit length [7]. This means that at all time only three of the quaternion elements can change freely while allowing for a total magnitude of one. This causes singularities arise in the UKF covariance matrix unless complex additional measures are taken [7] [8]. Additionally, values cannot be added to a quaternion as it is unit norm constrained which poses an extra challenge during the update step of the UKF.

Euler angles do not suffer from the singular covariance issue as they are a minimal attitude representation and are not unit norm constrained, however they do suffer from another form of singularity where in certain orientation two of the angles become indeterminate and can vary wildly with only small changes in attitude. This makes it very difficult for the UKF to converge on a solution.

Modified Rodriguez Parameters are related to the quaternion, but they represent the attitude in a minimal form using only three elements. This means that they do not result in a singular covariance matrix. Additionally, they are not unit norm constrained and only have a single singularity near the attitude represented by the quaternion as  $-1 + 0i + 0j + 0k$  where the MRP elements tend towards infinity. This requires a fix, but one which requires no conditions. Fortunately, for each MRP there is an equivalent, known as a shadow parameter, which has represents the same attitude but whose magnitude is inverted [7]. This allows you to swap between the MRP and its "shadow parameter" whenever its magnitude gets too large. This maintains a consistent attitude parametrization without ever getting near the singularity. The equation for converting between an MRP and its shadow parameter and vice verse is the following:

$$\mathbf{p}_{shadow} = -\frac{\mathbf{p}}{\|\mathbf{p}\|^2}. \quad (2)$$

The kinematic equations of motion for the Modified Rodriguez Parameters are as follows [9]:

$$\dot{\mathbf{p}} = \frac{1}{2} \left( \frac{1}{2} (1 - \mathbf{p}^T \mathbf{p}) \mathbf{I} + \mathbf{p}^\times + \mathbf{p} \mathbf{p}^T \right) \boldsymbol{\omega}. \quad (3)$$

### 2.3 Tumbling Formulation

In the case that the object is tumbling, that is to say that the angular velocity is not constant in the ECI frame, inertial properties need to be either known or estimated. If these properties are known then the state definition above suffices and only the forward propagation model must be changed. This is unlikely however as it is often difficult even for operators to accurately measure a spacecrafts inertial properties. This leads to the necessity to estimate the inertial properties.

This paper estimates the inertial properties by adding them to the state estimate of the UKF. This typically requires nine elements to fully define, which adds significantly more computational complexity to estimate. The ability to effectively represent the inertia of the object in the fewest number of parameters significantly reduces the number of calculations required.

It is possible to take advantage of the symmetric properties of the inertia matrix and add the matrices diagonal and only estimate the diagonal and either the upper or lower triangular. This only adds six elements to the state as opposed to nine, however this is still a significant jump in computational complexity and increases the difficulty for the UKF to converge on accurate values. This paper makes the following two assumptions to reduce the number of elements even further.

1. The principal inertial frame is sufficiently aligned to the frame in which the geometry is defined such that the off-diagonal elements are negligible. This allows for the off-diagonal elements to be assumed to be zero, reducing the elements required to be estimated to only the diagonal.
2. The disturbance torques applied to the spacecraft are negligible over the duration of a single pass. It can be shown that in the absence of disturbing torques the specific values of the inertia matrix no longer matter, rather it is only their relative magnitudes. This assumption is valid a wide range of spacecraft as the duration of a single pass is so small that very few torques could significantly affect measurements. This assumption allows for one element of the inertia matrix to be assumed to be one.

The combination of these two assumptions reduces the number of elements that needed to be estimated to two: the second and third diagonal elements. Given these assumptions, the state vector becomes:

$$\mathbf{x} = \begin{bmatrix} \mathbf{p} \\ \boldsymbol{\omega} \\ \boldsymbol{\Xi} \end{bmatrix}, \quad (4)$$

where  $\boldsymbol{\Xi}$  is defined to be a 2x1 vector containing two of the diagonal elements of the objects principal inertia matrix.

Light curves are the data collected by observing a satellite with a telescope and measuring the amount of light collected from it. In order to predict how much light a spacecraft is reflecting as a function of its attitude a reflection model is needed. This paper implements a modified version of the Phong Bi-Direction Reflection Distribution Function (BRDF) as used by Linares et. al [8] as well as a ray tracing algorithm that was proposed by Kaasalainen and Torppa [3].

An overview of the process is that there is a spacecraft geometry defined by a set of flat facets and at every measurement the facets that are both illuminated and visible by the observation site are evaluated by a BRDF. This BRDF takes into account the direction of the illumination source and observation as well as the illuminated area of the facet which is calculated using a ray tracing algorithm. The individual contributions of each facet are then summed to return the total reflected by the spacecraft.

All math for the measurement model can be calculated in any frame, however the author decided to work entirely within the spacecrafts body frame as this minimizes the number of rotations that need to be performed. Using the spacecraft body frame only requires that the observation and sun vectors be rotated rather than the entire spacecraft geometry.

### 3 Observation Model

According to Ashikhmin and Shirley, reflections can be modelled as the sum of their specular and diffuse components such that [10]:

$$\rho_{total} = \rho_s + \rho_d \quad (5)$$

All vectors in the following equations are used in the spacecraft body frame.

One feature of the BRDF used in this paper is the ability to model anisotropic reflection, meaning that it can model the "streakyness" of surfaces like brushed metal. However, this requires additional information to describe the distribution of this reflection. This paper assumes that the specular reflection is evenly distributed along all directions which allows the equation of specular reflection to be as follows [10] [4]:

$$\rho_{s_i} = \frac{n+1}{8\pi} \frac{(\mathbf{u}_{n_i} \cdot \mathbf{u}_h)^n}{\mathbf{u}_{n_i} \cdot \mathbf{u}_{sun} + \mathbf{u}_{n_i} \cdot \mathbf{u}_{obs} - (\mathbf{u}_{n_i} \cdot \mathbf{u}_{sun})(\mathbf{u}_{n_i} \cdot \mathbf{u}_{obs})} F_{reflect_i}, \quad (6)$$

where  $n$  is the specular distribution parameter, which this paper assumes has a value of 1. A realistic value for real materials is not specified in the original publication of the Phong model, nor in similar research applying it [10] [4] [11] [3].

The equation for  $F_{reflect_i}$  is [10]:

$$F_{reflect_i} = R_{spec_i} * (1 - R_{spec_i})(1 - \mathbf{u}_{sun} \cdot \mathbf{u}_h)^5. \quad (7)$$

Where  $R_{spec_i}$  is the specular coefficient for facet  $i$ .

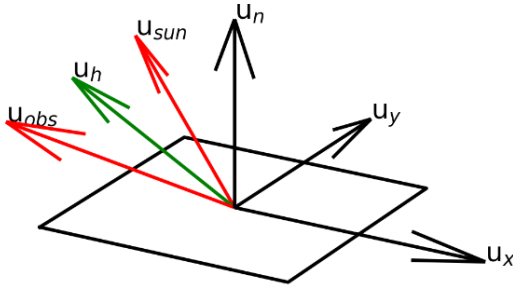


Fig. 1. Definition of vectors with respect to a facet.

For surfaces which reflect diffusely, the formula for the diffuse component is as follows [10] [4]:

$$\rho_{di} = \left( \frac{28R_{diffi}}{23\pi} \right) (1 - R_{speci}) \left[ 1 - \left( 1 - \frac{\mathbf{u}_{ni} \cdot \mathbf{u}_{sun}}{2} \right)^5 \right] \dots \left[ 1 - \left( 1 - \frac{\mathbf{u}_{ni} \cdot \mathbf{u}_{obs}}{2} \right)^5 \right] \quad (8)$$

Where  $R_{diffi}$  is the diffuse coefficient for the facet  $i$ .

This paper implements a geometric model which enables each surface of the object to be assigned a unique specular and diffuse coefficient. This enables the modeling of variegated surface coatings and varying materials.

The equation for the total visible power reflected by the spacecraft then becomes:

$$F_{obs} = \frac{C_{sun,vis}}{d^2} \sum_{i=0}^N A_i \rho_{totali} (\mathbf{u}_{ni} \cdot \mathbf{u}_{sun}) (\mathbf{u}_{ni} \cdot \mathbf{u}_{obs}) \quad (9)$$

Where  $C_{sun,vis}$  is the power flux output from the sun in the visible spectrum [455W/m<sup>2</sup>] [8].  $d$  is the distance from the observer to the spacecraft in meters,  $A_i$  is the illuminated area of facet (calculated by a ray tracing algorithm), and  $N$  is the number of facets.

This quantity is the basis for all observations, however data from collected in telescopes is rarely reported in Watts, but in either counts or intensity. Intensity is defined to be a logarithmic scaling of power, while counts is a linear scaling of the number of photons received by the CCD sensor during a single measurement. The conversion from Watts to intensity magnitude used in this paper is as follows [4]:

$$m = -26 - 2.5 \log_{10}(F_{obs}/C_{sun,vis}) \quad (10)$$

and the conversion from Watts to counts used in this paper is:

$$counts = \frac{F_{obs} \alpha \Delta t}{E_e - K} \quad (11)$$

Where  $\alpha$  represents the area of the telescope,  $\Delta t$  is the exposure time,  $E_e$  is the energy of a visible wavelength photon in Joules, and  $K$  is the CCD gain of the sensor [ $\frac{e^-}{count}$ ]. Either eq. 10 or eq. 11 should be used depending on the data.

## 4 Ray Tracing Model

As mentioned previously, the ray tracing algorithm is based on a description in Kaasalainen and Torppa [3]. This algorithm works by dividing each facet into sample grids, where the center of each grid is checked both for visibility by the observer and illumination from the sun. If either of these conditions is false then the area of the grid is not included in the total illuminated area. It is important to distinguish between body mounted facets and exposed facets (such as solar panels) as the backsides of body mounted facets are assumed to never be illuminated while exposed facets could be illuminated from either side. The backside of a face of a cube, for instance, is geometrically impossible to be illuminated from behind as its backside is completely hidden from the light source.

The first step is to iterate through each facet and precompute a list of other facets that could cast a shadow on them. When only rectangles are used, this implies checking the vertices of any potential occluding facets. If any vertex of facet B rises above the plane of facet A, then facet B is in the list of facets that could ever occlude A. This algorithm significantly reduces the number of facets that need to be checked, but it should be noted that it does not reduce it to the maximum extent. For example, this algorithm will include facets that may be separated by the body and in reality could never cast a shadow on one another. In the case of exposed panels, this paper assumed that all other facets could cast shadows.

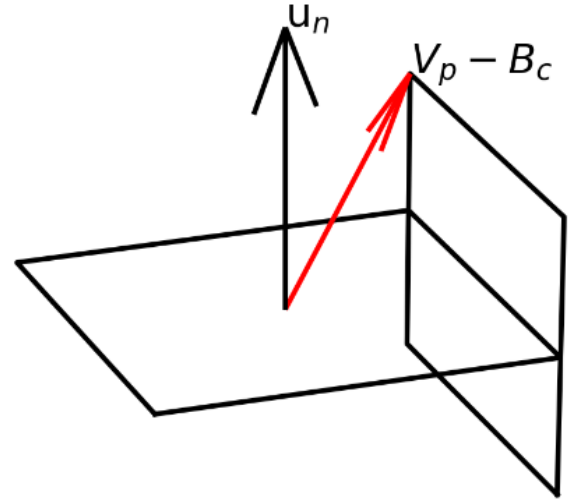


Fig. 2. Visualization of an occluding facet.

In order to estimate the area of a facet that is contributing to the measurement, regularly spaced sample points need to be precomputed across each face. Finer spacing will result in more accurate results but increase the computer time required. It is important that each sample point represents an equal area of the facet. To do this, sample points should be placed at the centers of grid squares of equal area.

When the visible brightness of any facet needs to be computed, these points will have to be checked for both vis-

ibility and illumination. A point is both visible and illuminated if all of the following conditions are met:

1.  $\mathbf{u}_{obs} \cdot \mathbf{u}_n > 0$
2.  $\mathbf{u}_{sun} \cdot \mathbf{u}_n > 0$
3. There is no facet between the point and the sun. (Shadow)
4. There is no facet between the point and the observer. (Hidden)

The last two rely on the vector-plane intersection equation.

$$d = \frac{(\mathbf{p}_0 - \mathbf{l}_0) \cdot \mathbf{n}}{\mathbf{l} \cdot \mathbf{n}} \quad (12)$$

Here,  $d$  is the distance between point  $\mathbf{l}_0$  and the plane defined by the normal vector  $\mathbf{n}$  along the vector  $\mathbf{l}$ .  $\mathbf{p}_0$  is a point on the plane. This equation will be used to determine the point of intersection of  $\mathbf{u}_{obs}$  and  $\mathbf{u}_{sun}$  from each sample point to the planes of each occluding facet.

As long as  $\mathbf{l}$  is not perpendicular to  $\mathbf{n}$  there always exists a distance  $d$ . This paper determines whether or not a ray intersects a facet within its boundaries by first calculating the point of intersection of the ray and plane using:

$$\mathbf{p}_x = \mathbf{l}_0 + d\mathbf{l} \quad (13)$$

This point of intersection is then recalculated from the center of the occluding facet and its projection along  $\mathbf{u}_x$  and  $\mathbf{u}_y$  are compared to the facets dimensions to determine if it hit within the edges of the facet.

The approximation of the total illuminated area of the facet then becomes:

$$A_i = A_{i0} \left( 1 - \frac{\text{number of points excluded}}{\text{total number of points}} \right) \quad (14)$$

Where  $A_{i0}$  is the total area of the facet. In the convenient case where a facet has no other facets that could occlude it,  $A_i = A_{i0}$ . This is true of every facet on a geometry which is a convex polyhedron.

## 5 Results and Analysis

### 5.1 Test Cases

The test cases looked at were selected to determine the effects of the spacecraft inertia, the spacecrafts orbit and its geometry. In total 18 total cases were simulated, each were simulated at various times of the year with randomized angular velocities.

The geometries used in this analysis were a rectangular prism, a cylinder, and a box-wing. The first two are convex geometries that have differing levels of symmetry, while the box-wing geometry is concave. These geometries can be seen in figure 4. The orbits examined are Low Earth Orbits (LEO), elliptical Medium Earth Orbits (MEO) and Geostationary (GEO). The final variable is the spacecrafts inertia.

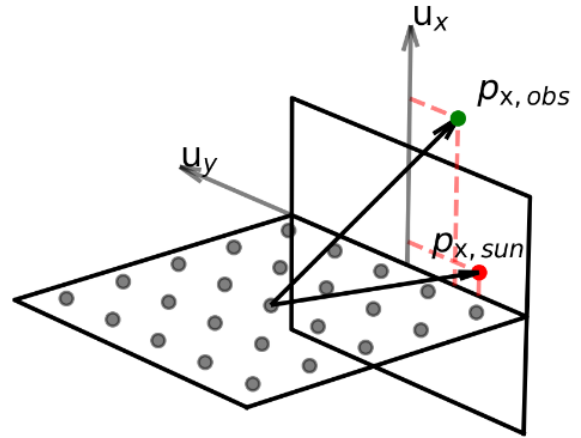


Fig. 3. A sample point that is visible but not illuminated

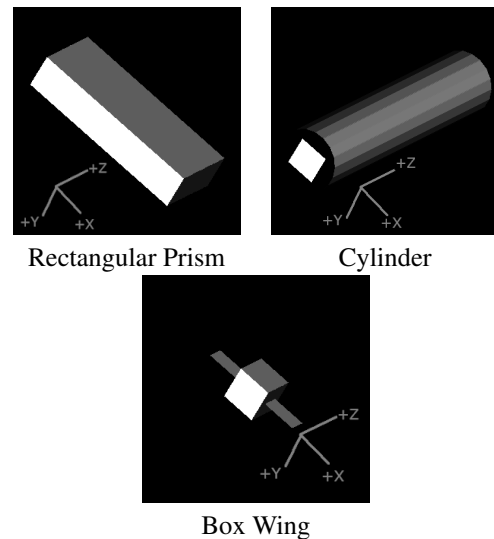


Fig. 4. Three Simulated Geometries.

Orbit	Ecc.	Semimajor Axis	Inc.	Period
LEO	0.0029	6,864 km	97.042	94 m
Ecc. MEO	0.5989	17,254 km	31.273	375 m
GEO	0.0001	42,164 km	0.028	1436 m

Fig. 5. Three Simulated Orbits.

In the first case, the principal inertial axes are assumed to be aligned with the spacecraft body frame and equal in magnitude. This corresponds to the inertial properties of a uniform sphere. The effect of this is to make the spin axis constant for all time. In the second case, the principal inertial axes are all different and are not aligned with the body frame, causing the spin axis to change over time.

### 5.2 Methodology

#### 5.2.1 Simulation Methodology

First, a LEO, MEO, and GEO orbit were selected. Passes were calculated by brute force sampling a spacecrafts

location and checking for necessary conditions. These conditions were obviously that the spacecraft must be above the horizon of the observation site and that the spacecraft be illuminated. Passes lower than 20 degrees elevation were discarded because of their decreased length. Additionally, because this paper assumed that atmospheric effect were negligible, low elevation passes violate this assumption. Additionally, in preliminary experiments it was noticed that the UKF often failed to converge to a solution when the angle between the observation and sun vector was greater than 90 degrees. This is likely because the probability of any facet to be illuminated and visible drops significantly as the illuminated faces become predominantly on the far side of the object. This increases the indeterminacy of the problem as sometimes as few as only one illuminated surface may be visible. Therefore passes whose observation and sun vectors were separated by more than 90 degrees were also discarded. Passes were also limited to only 5 minutes of data collection as MEO spacecraft passes can be hours long and geostationary passes are perpetual.

A 5 minute pass provides a significant amount of data, more than enough for the UKF to converge to a result. Additionally, based on the data provided by Lockheed Martin Space, real pass data is rarely collected for more than a few minutes.

Once a pass was identified, the spacecraft was given three initial attitudes and angular velocities between 0.1 and 0.3 radians per second. These were then propagated and used to calculate three different light curves per pass. Before entering the Kalman Filter, Gaussian noise was added to the light curve whose distribution was similar to that of the real data collected. Gaussian noise is standard as the assumption of the Kalman Filter is that the noise processes are distributed in a Gaussian manner [12]. The standard deviation seen in the real data varied typically between 1-30 counts, and so this range of values was used to generate the gaussian noise.

The simulated sample rate was 100 measurements per second or 0.01 seconds between measurements. This is significantly higher than the sample rates used by other researchers such as one sample every 1.316 seconds in Wetterer et. al [1] or one every 5 seconds in Holzinger et. al [2]. This was done to match the data provided by Lockheed Martin Space which contained a range of sample rates which were typically in the neighborhood of one sample every 0.025 seconds. This is quite a remarkable data rate.

The inertia matrix used for the spacecraft in the tumbling cases was as follows:

$$\begin{bmatrix} 1 & .01 & .01 \\ .01 & 2 & .01 \\ .01 & .01 & 3 \end{bmatrix}, \quad (15)$$

with the exception of the MEO and GEO box wing tumbling cases whose off-diagonal elements were set to zero.

These diagonal elements are each different, meaning that this object now has a minor, major, and intermediate axis

which leads to tumbling behavior. The off-diagonal elements reflect a rotation between the inertial axes and the geometric frame which was assumed to be negligible in the formulation. In the box wing MEO and GEO cases these are set to zero, meaning that the inertial axes are aligned with the geometric frame. In this case, the assumption that the off-diagonals are negligible is completely correct and the UKF can fully estimate the state.

This matrix follows the assumption used in the derivation of the UKF formulation which was that the off-diagonal elements are small and therefore negligible. It should be noted that the formulation used to estimate these parameters does not estimate the off-diagonal elements.

Both UKFs were initialized with an angular velocity of [0.01,0.01,0.01] and an initial Modified Rodriguez Parameter of [0.01,0.01,0.01]. These values were arbitrarily selected so as to give the UKFs no initial information about the objects state. It was also noticed that when given all zeros initially the UKF was much slower to reach an estimate.

The diagonal inertia terms were initially set to [1, 1]. Again these are simply arbitrary values in a reasonable range.

No differences were added to the geometric models between the data simulation and UKF analysis.

### 5.2.2 Convergence Criteria

Convergence was determined by examining the magnitude of the update to the angular velocity. If it was seen that the angular velocity was updated on average less than 1e-4 radians/second then it was said to have converged. For the real data the threshold of 2e-3 was applied to determine convergence. These values were empirically derived through guessing and checking.

For the cases where angular velocity was held constant, this resulted in very satisfactory results. However, in the cases where the angular velocity was not constant, the UKF would meet the convergence criteria without producing a realistic solution. The successful runs of the UKF for these cases were then hand selected using the criteria that a valid solution for angular velocity should appear sinusoidal and not change dramatically in amplitude or period.

This is likely due to the UKF's formulation as it is unable to completely estimate the inertia matrix. Therefore even when it converges to the correct angular velocity it deviates from this over time requiring relatively large update steps.

### 5.2.3 Data Filtering

When analyzing the data it is important to keep in mind that this problem is indeterminate and that multiple solutions are possible which are all equally plausible when the objects true attitude is not known. This poses a challenge in quantifying the performance of the UKF as the result can only be directly compared to the simulated truth when the UKF happens to converge to it rather than another equally plausible solution. When the UKF produces one of these alternate solutions, it cannot be compared to the simulated truth to measure accuracy. This would not be an issue if these alternate

solutions were the minority of solutions found as they could simply be discarded. However, these alternative solutions are by far the majority.

A known example of a solution which can never be discarded is the angular velocity corresponding to the negative of the truth. It is not possible to know whether an object spins clockwise or counterclockwise about any given axis using only light curve data [13]. Therefore, in this paper, only the axis of rotation is examined. What this means is that, during analysis, the estimated angular velocity was multiplied by 1 or -1 to minimize the dot product between the true angular velocity and estimated angular velocity. This simply serves to make valid results more apparent.

As can be seen in figure 6 by simply comparing the converged solution with the truth model the performance appears to be lousy. This does not make sense, as every converged solution successfully recreated the simulated lightcurve, meaning that it is a completely plausible solution.

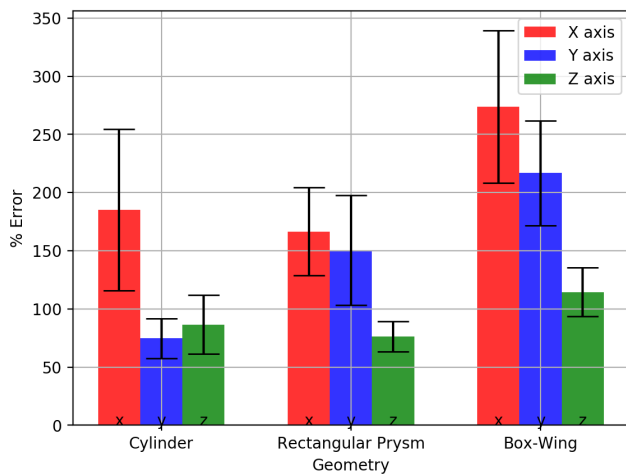


Fig. 6. Relative Error in the ECI Frame When Directly Comparing to Simulated Truth

What was assumed is that for any given simulated trial, for every axis there are multiple valid solutions and that if the data were filtered many times these solutions would each appear as a group of solutions centered on a mean with similar variances. A hypothetical example of this is shown in figure ???. These assumptions may not be valid. It may be that the solutions overlap significantly and it is not possible to separate them. However, in general once the UKF settled on a solution it showed a very small variance, making it likely that this assumption is true.

In order to yield meaningful results without reducing the sample size to only a handful of cases, the following methodology was applied to the data. **If any component of the angular velocity fell within 3 standard deviations of the ground truth, it was considered to be converging towards it and its error would be added to the statistics. This allows for an analysis to be conducted but does reduce the**

**strength of the results.**

### 5.2.4 The Observation Frame

Angular velocities were analyzed in two frames: the body frame and the observation frame. The body frame is the reference frame fixed to the spacecraft body, examples of which can be seen in figure 4. In this frame, direct comparisons can be made to the ground truth and deductions can be made about performance with respect to the spacecraft geometry. As it can be shown that multiple attitudes can result in the same light curve, the body frame serves as a poor frame to analyze angular velocities which may appear wildly different in body frame but which closely mirror the ground truth when the spacecraft attitude is accounted for.

Often, a solution may match the truth model much more closely in a frame that does not depend on the attitude of the object. An example of this can be seen in 13 where the angular velocity in the body frame is significantly more off than in the Observation Frame.

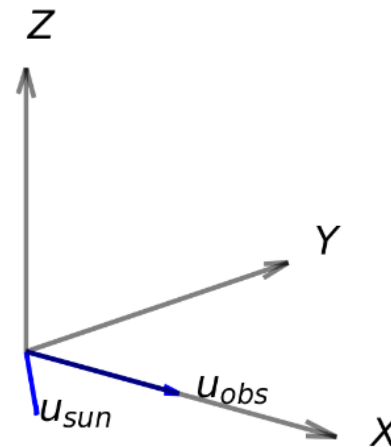


Fig. 7. Definition of the Observation Frame With Respect to the Sun and Observation Vectors.

The observation frame is defined to have its origin at the center of the spacecraft, its X axis along the observation vector, the Z axis being the cross of the sun and observation vector, and the Y axis completing the frame. This frame enabled comparisons between the estimated and true angular velocities in a frame which is irrespective of the spacecrafts attitude. Additionally, this frame allows for the error analysis with respect to the geometry of the situation. For instance, in figure 18 the observation frame reveals a solution which is unrelated to the model truth except that it is mirrored about the plane defined by the observation and illumination vectors.

## 6 Simulation Results

### 6.1 Existence of Multiple Solutions

The simulation results reveal that the problem of uniquely identifying an attitude profile from a light curve is an indeterminate problem. The data shows that for any light curve, there are multiple combinations of attitude profiles and angular velocities that can produce it. Many of these solutions are a result of the symmetry of the spacecraft.

The number of indistinguishable solutions could be reduced if the observed object has a highly asymmetric geometry or if its reflectance properties vary between panels. These two quantities both depend on the object and can be conveniently selected in simulations, however in reality many objects are highly symmetrical and the reflectance properties across the geometry would be unknown.

After seeing these results, one final run was conducted using the rectangular prism geometry in a geostationary orbit with each face having different reflectance properties. What was found was that the convergence success rate increased to 83%, however only 1 solution in 36 converged exactly to the simulated truth. The individual results were not significantly different than the other shown and so plots have not been included. The author would simply like to mention that this was investigated.

It should be carefully considered when selecting the reflectance properties of the spacecraft without complete knowledge. Any light curve can be recreated using any combination of geometry and reflectance properties [13]. Attempting to reduce the number of solutions in this way without knowledge of the true properties may result in the exclusion of correct solutions.

### 6.2 Hypothesis

This paper hypothesizes that a predicable set of solutions exists which can recreate a given lightcurve. This second set of solutions is characterized by an angular velocity vector whose magnitude and direction are directly mirrored across the XY plane of the observation frame.

It can be noticed in the formulation of the measurement model that measured light intensity is a function of the relative directions of the facet normals, observation, and velocity vectors. If sufficient symmetry exists within the spacecraft geometry such that it is possible to create what appears to be a reflection of the spacecraft geometry through only rotation, then this second set of solutions is expected to exist. This is because a mirroring of the spacecraft geometry about the XY plane of the observation frame preserves the angles between the sun, observation, and each facet normal vector.

This is only possible when the observational plane remains relatively constant however. As the observational plane changes, so must the mirrored angular velocity. As the UKF used in this paper assumes that the angular velocity is either constant or changes according to Eulers equations of rigid body motion. This un-modeled motion usually excludes the mirrored solution as valid.

### 6.3 Case 1: Fixed Axis of Rotation

It is seen in figure 8 that the UKF performs significantly better in the Geostationary cases. Excepting the cylinder case, where the LEO and MEO had similar success rates, it seems that LEO is the most challenging for the UKF.

This is likely due to the fact that in both MEO and LEO, the amplitude of the light curve can vary dramatically across the pass as the objects distance from the observer changes. This means that small errors in the state estimate correspond to different magnitude errors depending on when they occur during the pass. This is to say that the model uncertainty changes throughout the pass while the UKF assumes it is constant. The reason MEO performs better than LEO is because a MEO object near apogee has a very constant amplitude. In GEO, the spacecraft effectively do not change their distance from the observer and so their model uncertainty remains extremely constant.

Geometry	LEO	MEO	GEO	Total Trials
Cylinder	52.77%	48.88%	69.44%	117
Rectangular Prism	19.44%	57.77%	63.88%	117
Box-Wing	0.00%	50.00%	86.95%	80

Fig. 8. Percentages of Trials with Converged Solutions: Fixed Axis Case

It can be seen that in figure 9, the cylinder geometry had significantly better performance about its Z-axis which corresponds to its length. In figure 4 it can be seen that the cylinder is modeled as a set of flat facets. It is likely that as the number of facets increases that the error along the Z axis also increases. This is because as the cylinder rotates each facet brightens and then dims. A true cylinder with uniform albedo would not behave like this, instead it would maintain a constant brightness throughout its rotation about the Z axis. The approximation of the cylinder using a finite number of flat facets likely enabled higher performance than would be expected.

In general the box-wing geometry has large error compared to the other two in figure 9. It is likely that the significantly reduced error about the Y axis has to do with the placement of the panels. The Y axis of this geometry corresponds to the axis normal to the "wings". The box-wing geometry was also the smallest geometry and so the modeled noise affected the signal proportionately more, which would explain the overall higher uncertainty for this geometry.

Looking that the error in the Observation Frame performance in figure 10, the cylinder geometry performed significantly better than the other two. Potentially this is due to the fact to make large changes in the attitude without affecting the performance by changing its rotation about its Z body axis. This decoupling between attitude and lightcurve may decrease the potential for this geometry to become stuck in a local minimum.

Figures 11, 12, and 13 are an example of a converged trial for each geometry. These results contain the angular

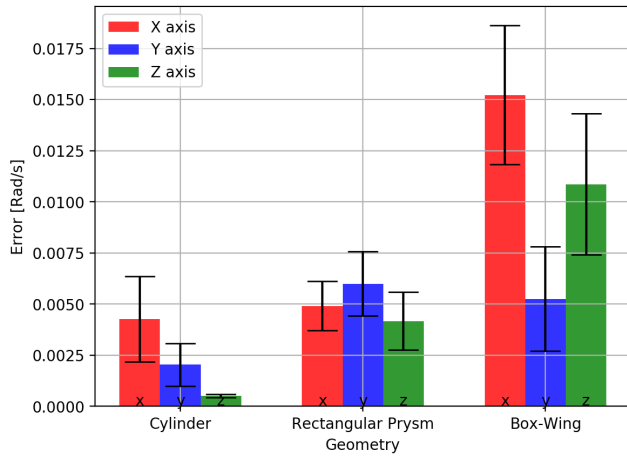


Fig. 9. Angular Velocity Error by Body Axis and Geometry With Data Filtering

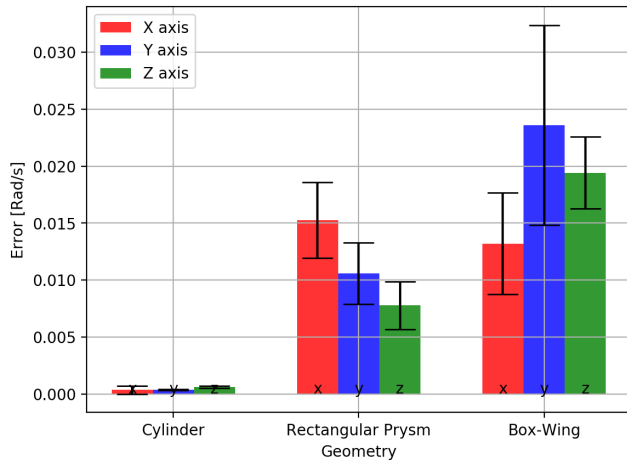


Fig. 10. Angular Velocity Error by Observation Frame Axis and Geometry With Data Filtering

velocity in the body frame as well as the observation frame so that the results may be compared directly as well as in a frame irrespective of the spacecraft attitude. The Light curve comparisons and residuals are also shown in the top left. The residual represents the difference between the estimated measurement and the true measurement. It can be seen in the residuals that once the angular velocities converge, the residuals also drop near zero with some variance which is largely a byproduct of the Gaussian noise added to the data. How close the residual is to zero is the only measurement of how well the state estimate matches the data. Finally, the Modified Rodriguez Parameters are included in the bottom right. These are included to show that solutions are found with entirely different attitudes than the truth but which still fit the data. It should be noted that the sudden jumps in both the true and estimated MRPs are simply the result of flipping between the MRPs and their shadow parameter as is described in eq. 2.

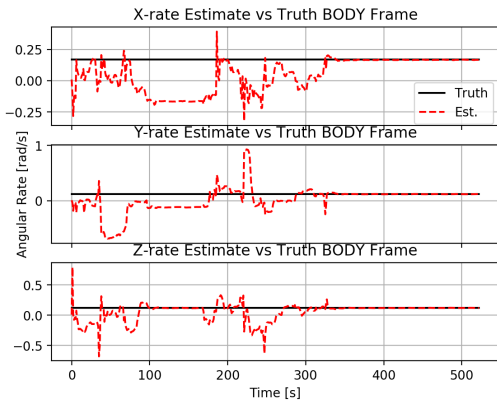
What you expect to see from a positive result in this case is the angular velocity in body frame to converge to fixed values and remain constant. In the Observation frame, it is not expected for the results to converge to a fixed value as the frame is non inertial. However, it is more likely for the estimated angular velocity to line up with the truth model in the observation frame and so it is expected but not required that a successful result match the truth model in the observation frame.

Additionally, a successful result is always expected to minimize the residual between the true lightcurve and the estimated light curve. Seeing the residual of the light curve comparison converge to a small number near zero is a sign of a valid solution regardless of the agreement between the modeled and true state.

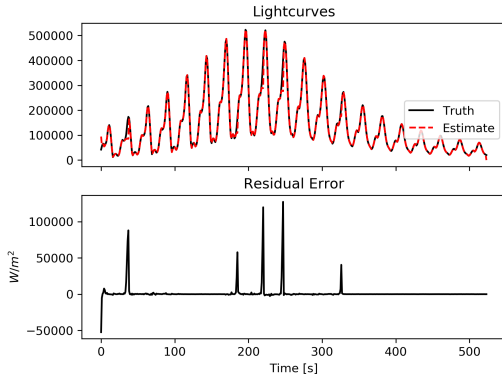
Finally, there is no expectation of the MRPs as in all cases there were multiple orientations which produced the same light curve. These results were included to show that there does not need to be any agreement between the true and simulated MRPs to produce a result that matches the data. If the problem were completely determinate the estimated MRPs would align with the simulated truth.

In this data we do see that the angular velocities converge to constant values which indicates success. Additionally when the estimate matches the truth in the observation frame it matches very closely. In all cases the residuals converge near zero. The variance around zero is largely due to the noise added to the measurements fed to the UKF.

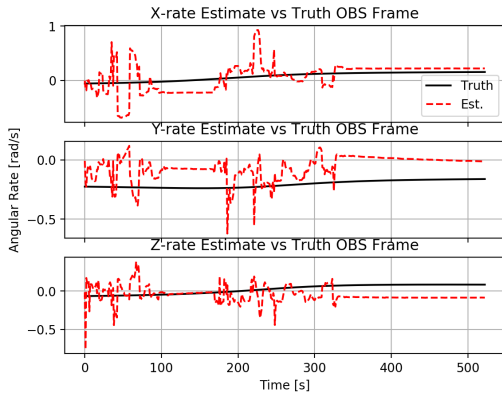
It is shown that there are multiple MRP solutions which can produce the same curve as in all three figures (11, 12, and 13) the MRPs converged to significantly different values.



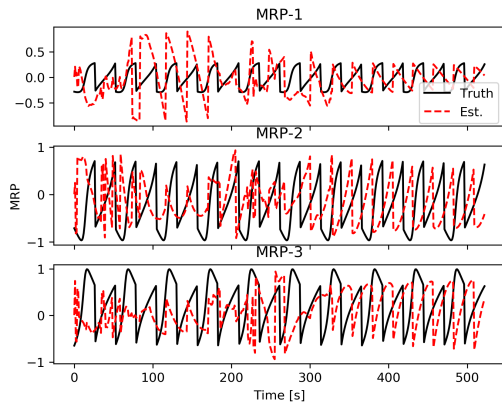
Angular Velocity in Body Frame



Light Curve Comparison

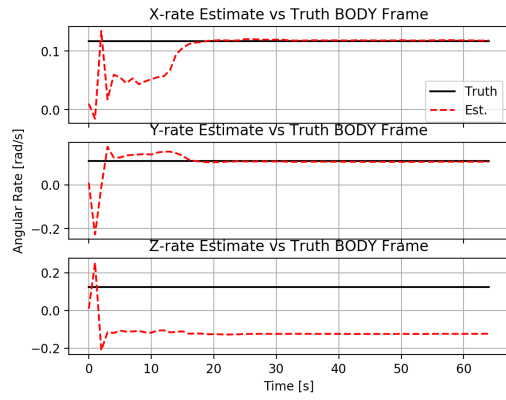


Angular Velocity in Observation Frame

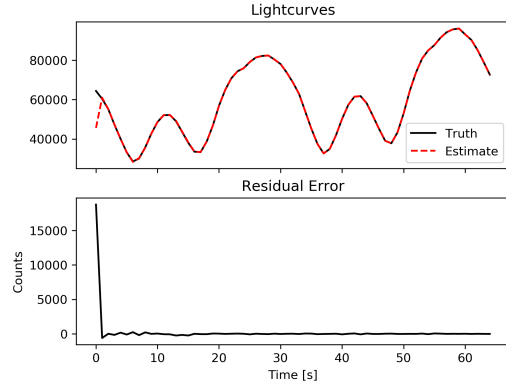


Modified Rodrigues Parameter Comparison

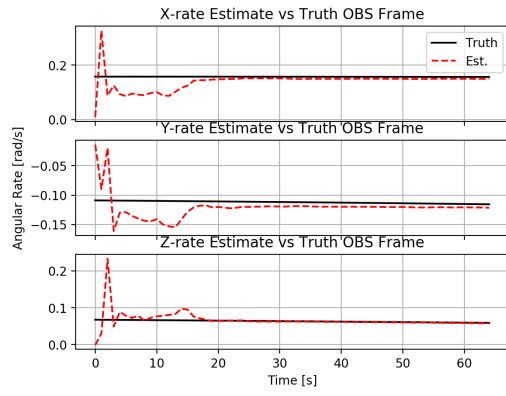
Fig. 11. Converged Solution of a Rectangular Prism in LEO spinning About a Fixed Axis.



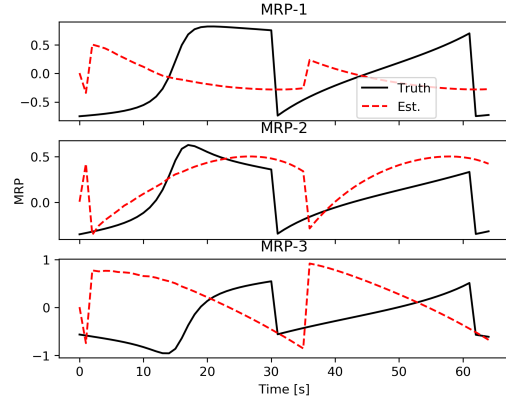
Angular Velocity in Body Frame



Light Curve Comparison

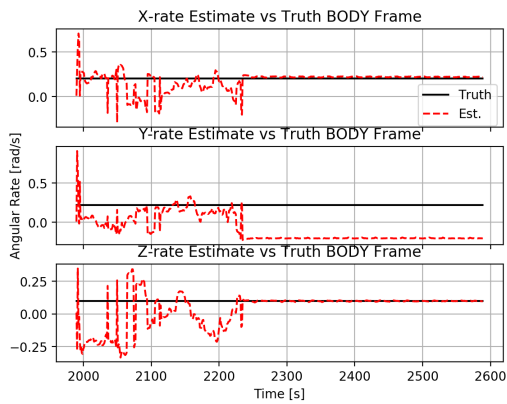


Angular Velocity in Observation Frame

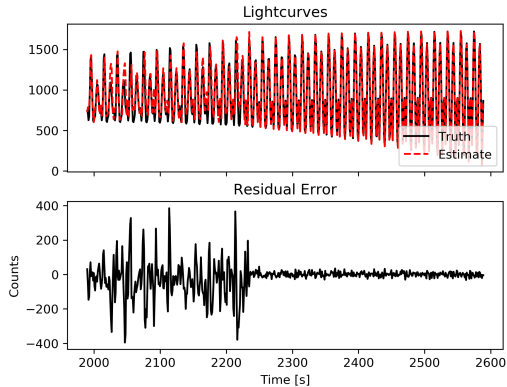


Modified Rodrigues Parameter Comparison

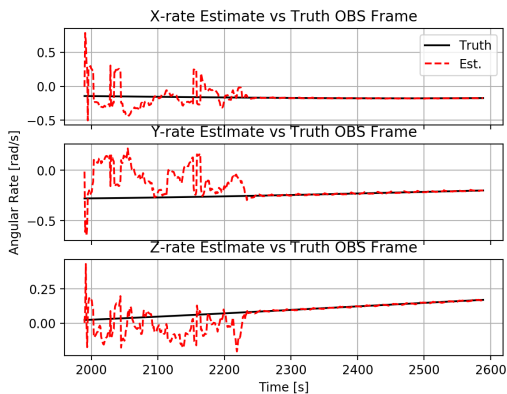
Fig. 12. Converged Solution of a Cylinder in LEO Spinning About a Fixed Axis.



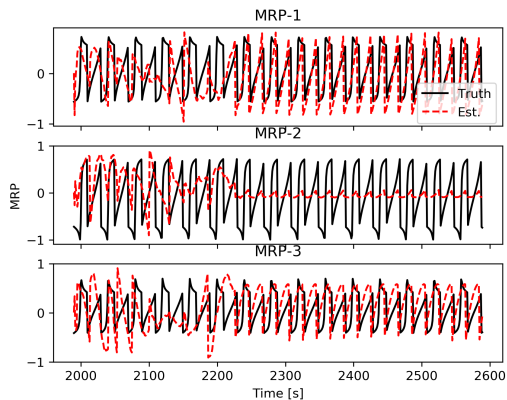
### Angular Velocity in Body Frame



### Light Curve Comparison



### Angular Velocity in Observation Frame



### Modified Rodrigues Parameter Comparison

Fig. 13. Converged Solution of a Box-Wing in GEO Spinning About a Fixed Axis

The formulation used in case 1 in which the angular velocity was assumed to be constant yielded very positive results with a solution being found in approximately half of the trials. Reiterating, these trials did not simulate geometric model uncertainty. This means that should this formulation be applied to real data the performance would be expected to decrease. Additionally, it is clear that any solution produced by any UKF is not unique. Figures 11, 12, and 13 demonstrate solutions which highly fit the data but are significantly different from the truth model.

## 6.4 Case 2: Tumbling Spacecraft

The success rates for the tumbling cases were far lower than in the fixed axis case as can be seen in figure 14. This is to be expected however as the number of parameters to estimate and the complexity of the models are significantly greater. Again though, we see the pattern in which performance increases with orbital altitude with GEO having the highest success rate and LEO having the lowest.

Geometry	LEO	MEO	GEO	Total Trials
Cylinder	22.00%	25.00%	25.00%	108
Rectangular Prism	2.77%	2.77%	16.66%	108
Box-Wing	0.00%	*0.00%	*41.37%	101

\* Spacecraft truth model had no off-diagonal elements.

Fig. 14. Percentages of Trials with Converged Solutions: Tumbling Case

Another trend which has continued into the tumbling case is that there are once again multiple solutions which result in the same predicted measurement. In this new data we see solutions converging with variations in period and amplitude in addition to magnitude and direction. These extra degrees of freedom could potentially be why the UKF struggles to settle on a single solution.

In regards to the Inertia estimation, results varied wildly. It is known that in the absence of disturbances only the relative magnitude of the inertia values matter. The top left element was forced to be 1, and the other two diagonal elements were expected to converge to the true values.

Figures 15, 16 and 17 are examples of converged results for each geometry. What is shown are the angular velocities in body and observation frame, comparisons to the predicted and measured light curve, and the values of the estimated inertia parameters. Only the inertia's about the Y and Z axes are shown as in the formulation the X axis parameter is forced to be 1 and is not estimated. Off-diagonal elements are not estimated and so are not shown.

In this case it is not expected that the angular velocity converge to a constant value since the spacecraft is tumbling. Instead it is expected to converge to some continuous curve. The inertia parameter are expected to converge to constant values.

Here as in the case of the fixed axis the residual is the

only measurement of how well the state estimate fits the data. The residual is simply the difference between the light curve generated by state estimate and the true lightcurve. A positive result is expected to have a residual converge near zero.

The MRPs were not included in these results as figures 11, 12, and 13 show that the attitude of the spacecraft could be any number of possible solutions and the same was seen in the tumbling cases.

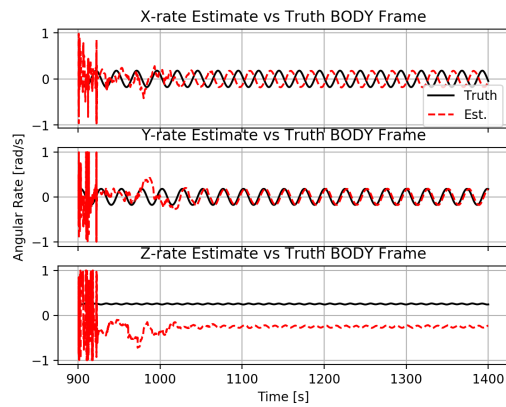
Indeed we see that in the converged cases the angular velocities in the body frame converge to continuous, periodic curves. In the body frame they seem to have some relationship but do not match. No trial run showed a perfect match between the angular velocity in either the body or observation frame.

In figures 15 and 16 it appears that in the body frame the UKF has converged to a solution which is related to the truth as each has one axis that aligns very well with the truth while the other two seem to be 180 degrees out of phase. In figure 17 the body frame rate estimates seem to imply the UKF becoming stuck in a local minimum as its angular velocity in the X axis seems to be in resonance with the true rate. It can be seen that for ever 4 periods of the true solution the estimated solution has completed 5.

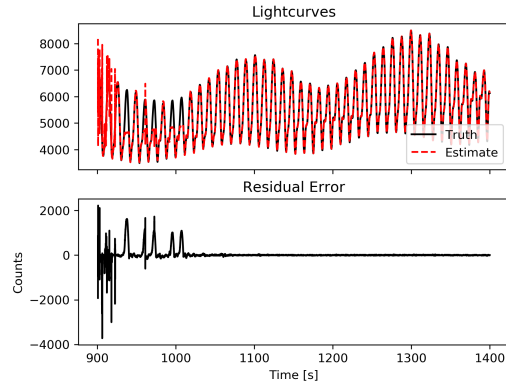
Unlike in case 1 where the axis of rotation was fixed, there is no clear deduction to be made from the angular velocities in the observation frame. Figures 15 and 16 seem to show some kind of reflection about the Z axis of the observation frame, implying some kind of geometric relationship between the estimated solution and the true solution. However, there is no clear alignment in the X and Y axes in either of these figures which was typical of solutions whose angular velocity was reflected about the plane of observation in case 1.

The performance of the residuals in the case 2 are also visibly worse when compared to the results of case 1. In figure 17 the residual is on the order of the measurement which signals that this result is simply the product of the UKF falling into a local minimum. Figure 17 is an example of a trial which converged but matched the data very poorly as it seems to have become "stuck" in a solution whose angular velocity has resonance with the truth.

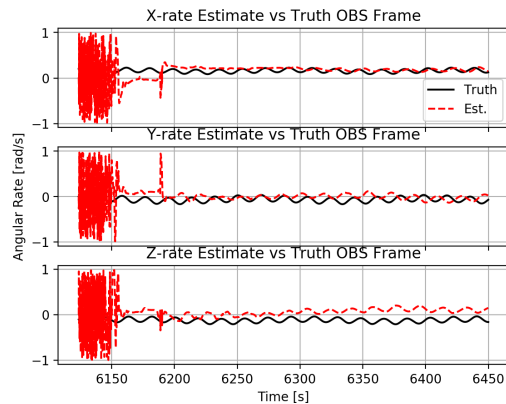
In terms of the inertia estimations, it is seen in figures 15, 16 and 17 that the inertia does indeed converge to constant values, although they are not as constant as the angular velocities were in case 1. It is interesting to note that in figure 17 the X axis inertia was estimated to be intermediate axis as the Y axis value was estimated to be less than one. In figures 15 and 16 the X axis inertia is correctly estimated to be the minor axis as the other inertia parameters are greater than 1, however in both figures the Y axis parameter was determined to be the major axis and the Z axis was determined to be the intermediate axis. This is determined by their relative magnitudes, in both cases  $Y > Z > X$ . By looking at figure 15 it can be seen that this is incorrect. Both of these solutions minimized the residual and can be considered valid results, meaning that once again, there are multiple possible solutions for the inertial parameters that can match the data.



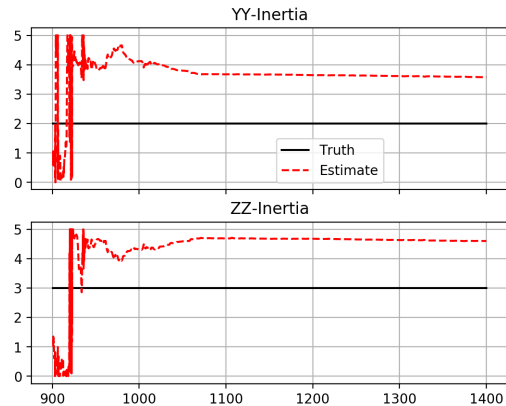
Angular Velocity in Body Frame



Light Curve Comparison

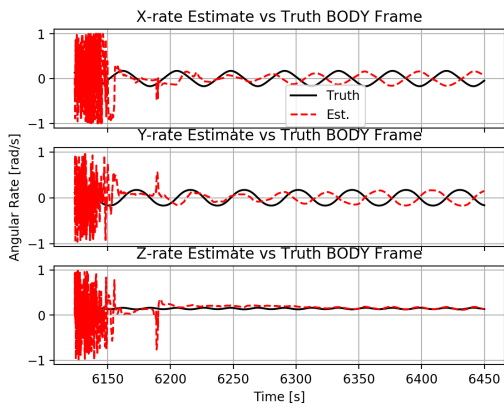


Angular Velocity in Body Frame

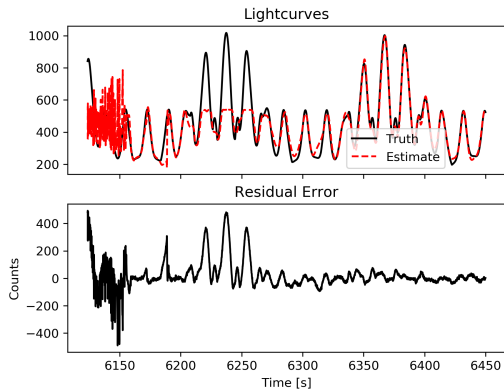


Estimated Inertia Values

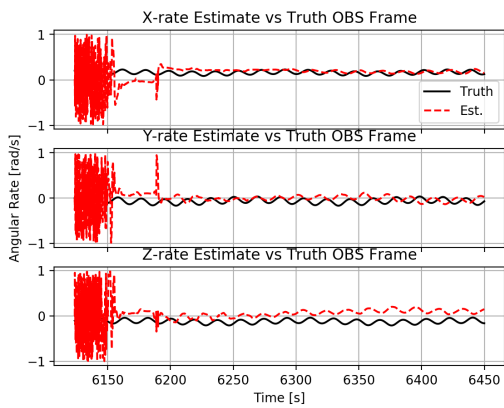
Fig. 15. Converged Solution of a Cylinder in MEO Tumbling.



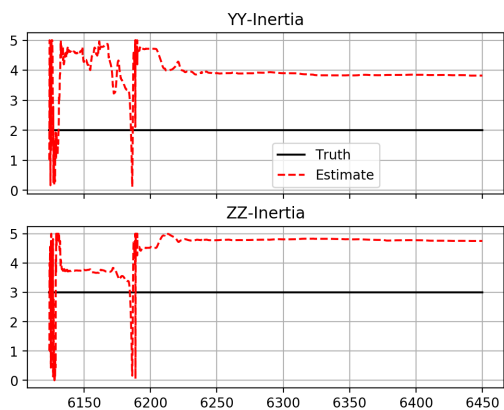
### Angular Velocity in Body Frame



### Light Curve Comparison

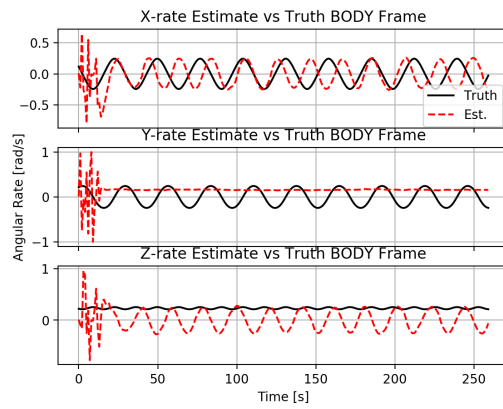


### Angular Velocity in Body Frame

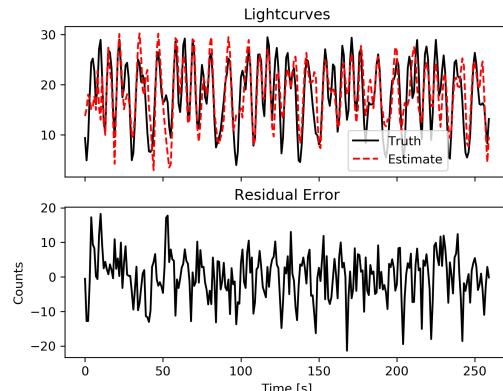


### Estimated Inertia Values

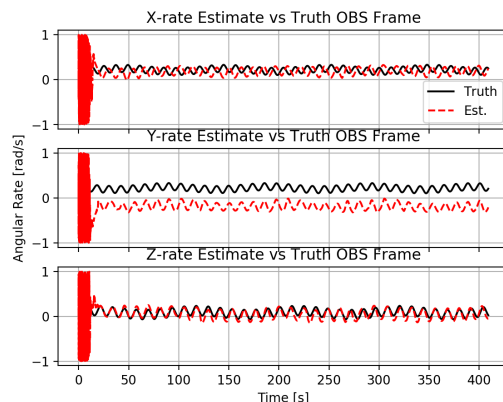
Fig. 16. Converged Solution of a Rectangular Prism in MEO Tumbling.



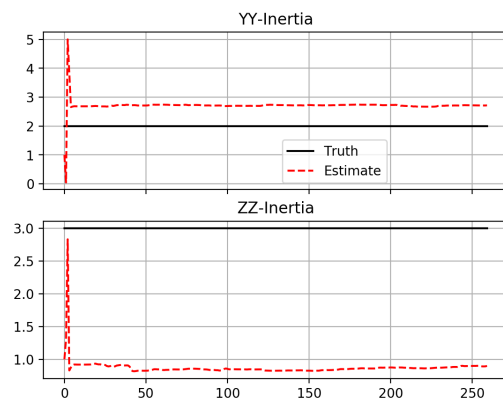
### Angular Velocity in Body Frame



### Light Curve Comparison



### Angular Velocity in Body Frame



### Estimated Inertia Values

Fig. 17. Converged Solution of a Box-Wing in GEO Tumbling.

The UKF formulation in which only two inertia parameters were estimated was able to converge to solutions which fit the data for all three geometries. However, the success rate was significantly low. This could potentially be improved slightly through tuning, however this formulation cannot fully estimate the inertia parameters which significantly reduces its ability to converge to a solution. Should this formulation be applied to real data it should be noted that the solutions produced are not unique and it is possible for the UKF to become stuck in a locally optimal solution which fails to fit the data.

## 6.5 Hypothesis Results

By examining the angular velocities in the observation frame, it was observed that 6 of the 314 trials converged to a solution which was mirrored across the observational plane. This was apparent because, in the observation frame, the angular velocity converged to the correct axis and magnitude with the exception that the Z component was the negative of what the truth.

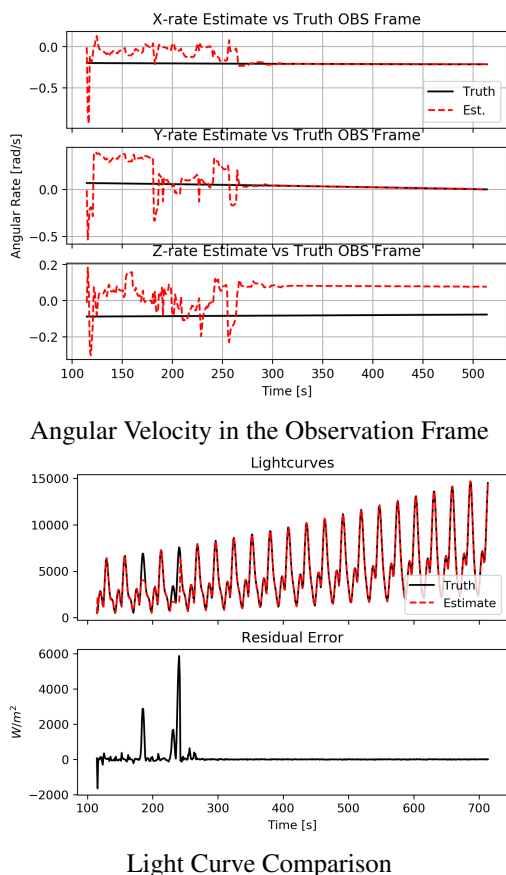


Fig. 18. Example of a solution which is flipped across the observation plane.

In figure 18 it can be seen that the angular velocity estimate converges to ground truth except for along the Z axis, where it converges to the negative. This corresponds with a



Fig. 19. Consecutive Images from the observers perspective of truth [TOP] and estimate [BOTTOM] showing a mirror image solution.

mirroring of the angular velocity about the XY plane of the observation frame.

In figure 19 a visualization is shown of the truth and estimated spacecraft attitudes. Here the symmetrical relationship between the true attitude and its mirrored counterpart. Additionally, it can be seen in figure 19 that the light curve is nearly identical to the original, suggesting that these two solutions are indistinguishable.

This result is important because as there are so many ways in which this attitude estimation problem are indeterminate. Any way in which a result can be predictably associated with a set of other potential solutions significantly increases the utility of the analysis. Knowing that this additional solution is possible allows for any single solution to now represent at least four alternative solutions which are simple transformations of each other. These 4 solutions are then the true angular velocity, its reflections, and their negatives.

## 7 Real Data

### 7.1 Real vs Simulated Data

It is noted that the real data looks significantly different than the simulated data. The simulated data has clearly defined, macroscopic, periodic variations which can clearly be attributed to a rotating, reflecting surface. The real data, which can be seen in Appendix B., is much more ambiguous. It is unknown if the high frequency variations in the data are noise or signal. A Fourier transform of the data did not show any frequency being significantly dominant.

The UKF largely ignored this high frequency variation and instead appeared to track the mean.

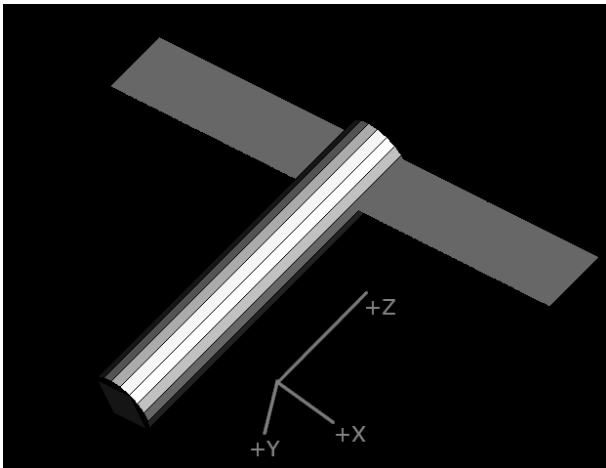
### 7.2 SERT-2

The Space Electric Rocket Test II (SERT-2) is a modified Aegena rocket body whose mission was to test two ion propulsion systems on board [14]. In order to power these propulsion systems, two deployable solar panels were added to the Aegena rocket body whose dimensions were 1.5x6 meters. The dimensions of the Aegena module were also 1.53x6 meters.

SERT-2 was launched on February 3rd, 1970 and was finally decommissioned in 1991. Due to the age of the spacecraft and considering that there is potentially fuel remaining within the Aegena tank, this spacecraft can be assumed to be spinning about its major axis. This simplifying assumption allows for the implementation of the simpler UKF formulation where no inertial parameters are estimated.



SERT-2, Source: NASA



SERT-2 Reflectance Model

Fig. 20. SERT-2 vs Reflectance Model

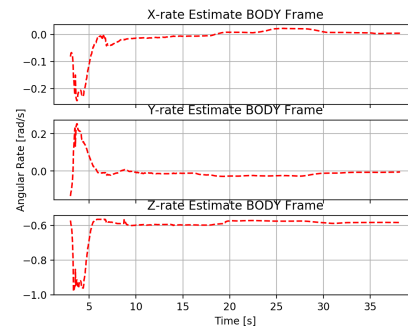
The geometry of SERT-2 is essentially a cylinder with two rectangular panels radiating from one end. This model is non-convex which means that it can take advantage of ray tracing algorithm described in this paper.

The geometric model for SERT-2 can be seen in figure 20. The reflectance properties used for each panel were a specular reflectance of 0 and a diffuse reflectance of 0.002. This reflects the properties of matte paint which reflects entirely diffusely. The diffuse coefficient value seems low, although a realistic range of values is not described in the original publication of the Phong model, nor is it described in similar research applying the Phong model [10] [4] [11] [3]. This value was empirically estimated to best fit the measured data.

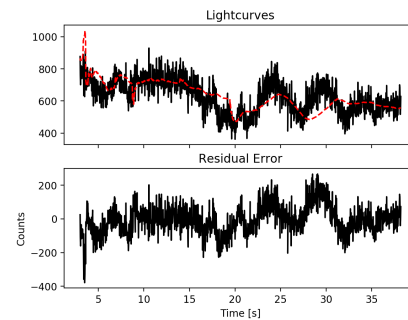
In figure 21 the results from one set of data are shown. These are presented in nearly the same manner as the trials in case 1 of the simulated trials. Here the angular velocity is presented in the body frame and the ECI frame (rather than the observation frame). The comparison between the light curve produced by the state estimate and the real data rare shown in addition to their residual. Finally, the MRPs are provided.

In this case the only quantity which can be compared are the measured light curve and the one generated by the state estimate. By looking at the light curve comparison it can be seen that the estimated state was generally able to predict the macroscopic trends of the data. This is a promising result which implies at least some success.

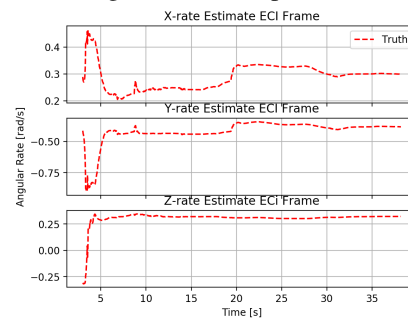
The angular velocities in both the body and ECI frame both converge to fairly constant values which is expected. Additionally the MRPs settled into a stable set of solutions. The strange behavior around 20 seconds in the MRP plot is caused by the UKF updating the MRP estimate very near the threshold of the flip from MRP to shadow parameter causing it to switch back and forth.



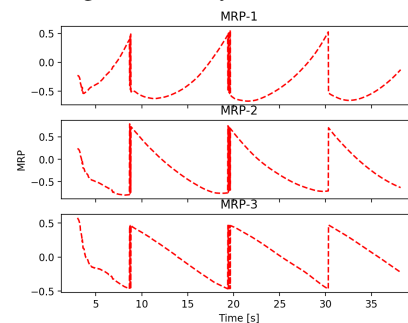
Angular Velocity in Body Frame



Light Curve Comparison



Angular Velocity in ECI Frame



Modified Rodrigues Parameter Estimates

Fig. 21. Convergence of a solution using real data of SERT-2.

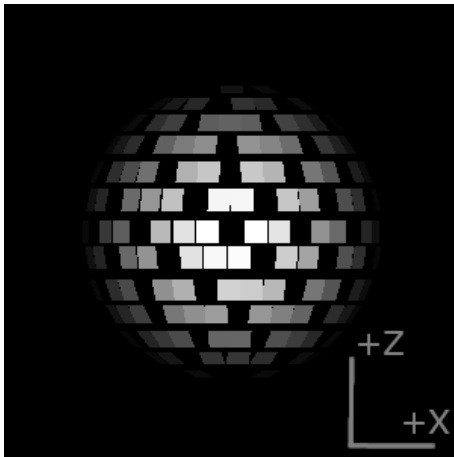
### 7.3 Ajisai (EGS)

Ajisai was a mission launched on August 13th, 1986 and was primarily intended as a dummy payload for the H-I launch vehicle. [15] Ajisai is essentially a sphere covered with 1,436 corner cube reflectors and 318 mirrors. [16] Its secondary mission (after being mass) was to determine the exact position of the more isolated Japanese islands. [15]

Because this spacecraft is so old and because it is a sphere, it is highly likely that it is spinning about its major axis and the simpler UKF formulation can be applied once more.



AJISAI, Source: JAXA



AJISAI Reflectance Model

Fig. 22. AJISAI vs Reflectance Model

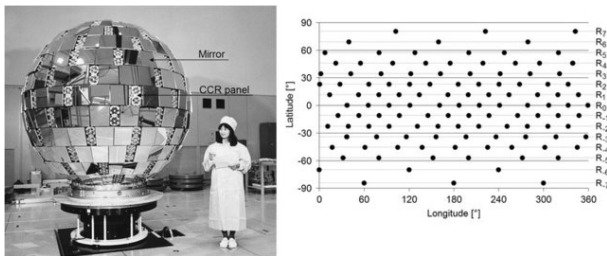
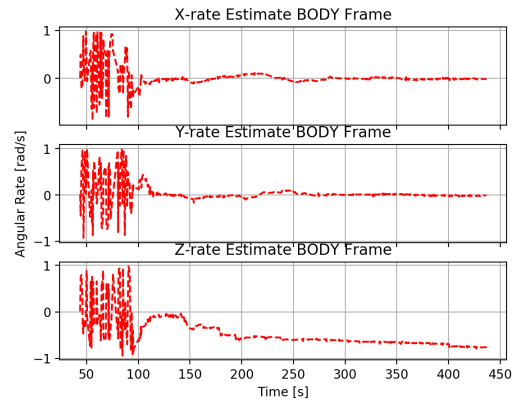
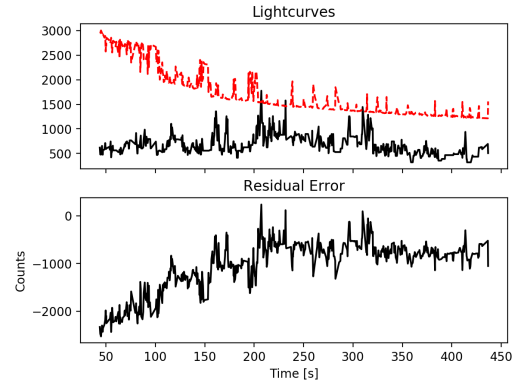


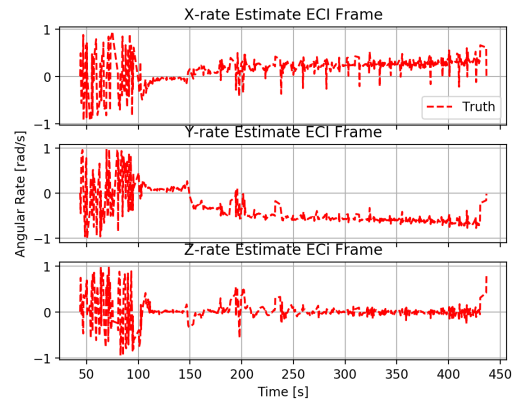
Fig. 23. AJISAI with Engineer [Left]. Corner Cube Reflector Locations [Right] [16]



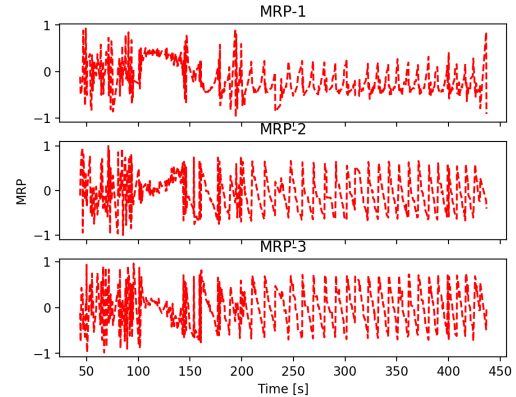
Angular Velocity in Body Frame



Light Curve Comparison



Angular Velocity in ECI Frame



Modified Rodrigues Parameter Estimates

Fig. 24. Measurement model mismatch with real data from AJISAI.

The geometry of the spacecraft is simply a large set of reflective panels. Being mirrors, these panels will have very high specular reflectance and almost no diffuse reflectance. The corner cube reflectors designed to reflect light back to its source. In this scenario, that source is the sun, and so the corner cube reflectors can be assumed to contribute nothing to the lightcurve. Thankfully, the positions of each corner cube reflector were documented, and the panel locations can be inferred from them.

The reflective properties used in this spacecrafts model was as specular reflectance of 0.002 and a diffuse reflectance of 0. These values were empirically estimated to best fit the measured data. It can be seen in figure 24 that the measurement model was unable to find an attitude which could recreate the magnitude of the measured data. This was the case for all attempts to filter data collected from this spacecraft.

Had the measurement model agreed with results, it still would have been a challenge for the UKF to converge to an accurate solution as AJISAI is roughly a sphere and its light curve is expected to vary only slightly as a function of attitude. Very high quality data would be needed to capture the detail necessary to discern attitude.

Figure 24 shows a trial with AJISAI data in which a solution was found but which did not fit the data. This is due to the large discrepancy between the true optical properties and the ones assigned to the model. It can be seen that even though a constant angular velocity is reached in the body frame, the light curve generated by this state estimate is significantly off from the real data. Additionally, by looking at the angular velocity in the ECI frame, it can be seen that the UKF had difficulty converging to a set of MRPs. It is likely that the attitude converged upon simply minimized the total brightness.

#### 7.4 Second Stage Ariane-40 R/B

The final object analyzed in this paper was the second stage of an Ariane-40 rocket. This particular rocket body was launched on September 26th, 1993 [17]. Roughly speaking, the geometry of this debris is roughly cylindrical and be expected to be rotation about its major axis. Therefore the same UKF formulation was applies as the previous two objects. Additionally, being a rocket body, fuel left over is expected to be removing kinetic energy through friction which increases the likelihood that it is spinning about its major axis.

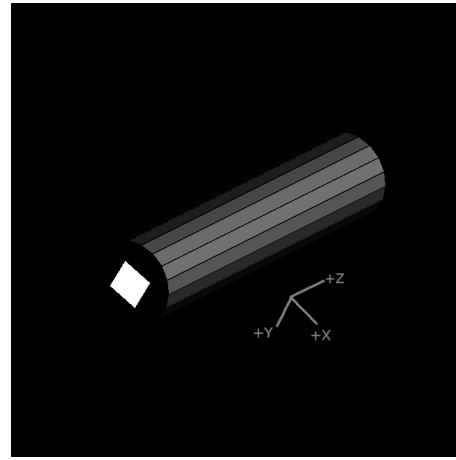


Fig. 25. Ariane-40 R/B Reflectance Model

The reflectance properties used for this model were, once again, a specular reflectance of 0 and a diffuse reflectance of 0.002 . These values were empirically estimated to best fit the measured data.

The UKF managed to converge to a solution in 6 of the 8 trials. Figure ?? shows the final angular velocities for the Ariane-40 R/B trials. It can be seen that in the body frame the majority of the solutions primarily lie along the Z axis. This is unsurprising as the Z axis of a cylinder has the least effect on the light curve. This means that there should be a large uncertainty about this axis leading to larger values.

Given the results of the simulated results presented in case 1, it was shown that the cylinder geometry had the smallest uncertainty about the Z axis. This is believed to be due to approximating the geometry with a small number of flat surfaces. Therefore the results from the case 1 trials cannot be used to interpret the data. Not only is this low uncertainty about the Z axis an artifact of approximation, the real object being studied is a true cylinder not a series of flat surfaces. The effect of approximating a cylinder with multiple surfaces is unknown.

In figure 26 the results from one set of data are shown. These are presented in nearly the same manner as the trials in case 1 of the simulated trials. Here the angular velocity is presented in the body frame and the ECI frame (rather than the observation frame). The comparison between the light curve produced by the state estimate and the real data rare shown in addition to their residual. Finally, the MRPs are provided.

It can be seen that the UKF does find a solution which minimized the residual, however the data provided for this spacecraft was mostly very flat. This is likely due to the spacecraft spinning so slowly that variations in the data are lost in the noise.

This limits the interpretability of the results, as the signal is so faint that it is unlikely to be sufficient for concrete results. However, the UKF does converge on a solution with near zero angular velocity in the X and Y body axes and only angular velocity in the Z axis. Again, the Z axis in the

body frame corresponds to the length of the cylinder and is expected to have a minimal effects of the light curve.

## 8 Conclusion

Two UKF formulations were derived to estimate the angular velocity of spacecraft using only light curve data. One formulation focused on the case in which the object is expected to be spinning about a constant axis, while the other accounted for the potential of the spacecraft to be tumbling. Both formulations were assessed using simulated light curves and the former was applied to real data which was collected and provided by Lockheed Martin Space.

On the simulated data it was shown that in the case of the object spinning about a fixed axis, solutions were converged upon for a the majority of the trials. For the trials in which the spacecraft was tumbling the success rates were significantly lower and varied significantly with respect to the objects geometry and orbit.

Overall it was noticed that both formulations performed significantly better when the object being analyzed was in a geostationary orbit where the amplitude of the light curve varied little. It was also noticed that performance varied significantly with respect to the presence of geometry features.

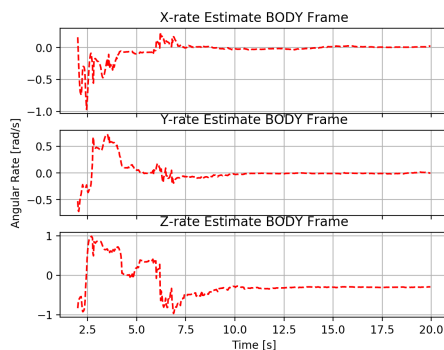
A novel result of this paper is the existence of a second group of solutions. It was found that for some angular velocity solutions, there is another solution which is simply the reflection of the first solution about the plane defined by the observation and sun vectors. This is interesting as it adds another element of uncertainty for any solution which is verified by simply comparing the produced light curve. It also allows for a single any single solution to potentially represent a family of solutions which can be easily checked without using brute force methods.

Solutions were converged upon when real data was analyzed, however it is unlikely that these solutions are correct and they cannot be verified. It was also discovered that there was a significant discrepancy between the light reflectance model used by the UKF and the real data collected. The reflectance properties of each spacecraft had to be significantly lowered in order to match the magnitude of the real data.

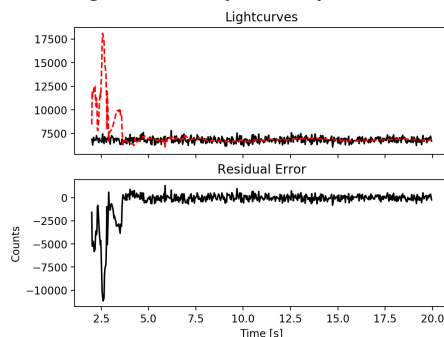
This paper attempted to create the simplest possible UKF formulations which would produce meaningful results. The belief was that by minimizing the number of parameters estimated, the fewer data would be required to converge on a solution as high quality data is usually scarce. This was accomplished, however the performance in the case of tumbling objects was very poor and the process of manually selecting the reflectance properties of the spacecraft were coarse and left much to be desired. When the off-diagonal elements were removed from the truth model, the tumbling UKF formulation improved significantly although too few trials were conducted without them to say so definitively. It is likely worthwhile to expand the estimated state to include a representation of the full inertia matrix.

## Acknowledgements

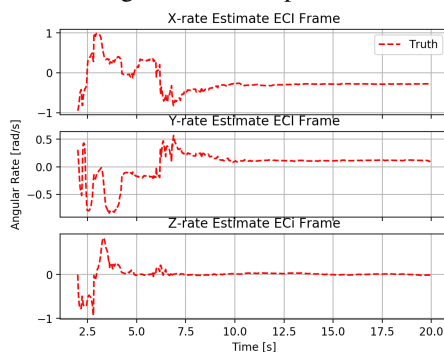
I would like to thank Lockheed Martin Space for their generous donation of such plentiful and high quality data. Additionally, thank you to Dr. Kira Abercromby for being the best advisor one could ask for during these trying times.



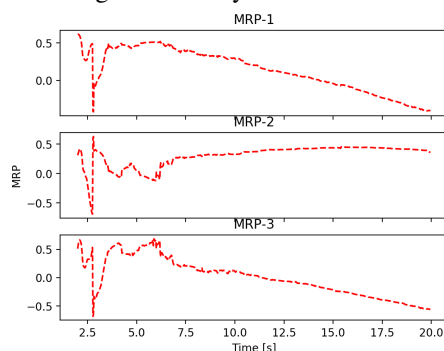
### Angular Velocity in Body Frame



### Light Curve Comparison



### Angular Velocity in ECI Frame



### Modified Rodrigues Parameter Estimates

Fig. 26. Convergence of a solution using real data of Ariane-40 R/B.

## References

- [1] Wetterer, C. J., and Jah, M. K., 2009. "Attitude estimation from light curves". *Journal of Guidance, Control, and Dynamics*, **32**(5), pp. 1648–1651.
- [2] Holzinger, M., Alfriend, K. T., Wetterer, C. J., Luu, K. K., Sabol, C., Hamada, K., and Harms, A., 2012. "Attitude Estimation for Unresolved Agile Space Objects with Shape Model Uncertainty". In *Advanced Maui Optical and Space Surveillance Technologies Conference*, p. 25.
- [3] Kaasalainen, M., and Torppa, J., 2001. "Optimization methods for asteroid lightcurve inversion: I. shape determination". *Icarus*, **153**, 09, p. 24–36.
- [4] Linares, R., Jah, M. K., Crassidis, J. L., and Nebelecky, C. K., 2014. "Space object shape characterization and tracking using light curve and angles data". *Journal of Guidance, Control, and Dynamics*, **37**(1), pp. 13–25.
- [5] Linares, R., Jah, M., and Crassidis, J., 2012. "Inactive space object shape estimation via astrometric and photometric data fusion". *Advances in the Astronautical Sciences*, **143**, 01, pp. 217–232.
- [6] Fulcoy, D. O., Kalamaroff, K. I., and Chun, F., 2012. "Determining basic satellite shape from photometric light curves". *Journal of Spacecraft and Rockets*, **49**(1), pp. 76–82.
- [7] Terzakis, G., Lourakis, M. I. A., and Ait-Boudaoud, D., 2017. "Modified rodrigues parameters: An efficient representation of orientation in 3d vision and graphics". *Journal of Mathematical Imaging and Vision*, **60**, pp. 422–442.
- [8] Linares, R., Jah, M. K., Crassidis, J. L., Leve, F. A., and Kelecy, T., 2014. "Astrometric and photometric data fusion for inactive space object mass and area estimation". *Acta Astronautica*, **99**, pp. 1 – 15.
- [9] Crassidis, J., and Markley, L., 1996. "Attitude estimation using modified rodrigues parameters". *Proceedings of the Flight Mechanics/Estimation Theory Symposium*, 01, pp. 71–83.
- [10] Ashikhmin, M., and Shirley, P., 2000. "An anisotropic phong brdf model". *J. Graph. Tools*, **5**(2), Feb., pp. 25–32.
- [11] Jah, M., and Madler, R., 2007. "Satellite Characterization: Angles and Light Curve Data Fusion for Spacecraft State and Parameter Estimation". In *Advanced Maui Optical and Space Surveillance Technologies Conference*, p. E49.
- [12] Kalman, R. E., 1960. "A new approach to linear filtering and prediction problems". *Transactions of the ASME—Journal of Basic Engineering*, **82**(Series D), pp. 35–45.
- [13] Magnusson, P., Barucci, M. A., Drummond, J. D., Lumme, K., and Ostro, S. J., 1989. "Determination of pole orientations and shapes of asteroids". In *Asteroids II*, R. P. Binzel, T. Gehrels, and M. S. Matthews, eds., pp. 67–97.
- [14] Kerslake, W. R., and Ignaczak, L. R., 1993. "Development and flight history of the sert ii spacecraft". *Journal of Spacecraft and Rockets*, **30**(3), pp. 258–290.
- [15] JAXA. About experimental geodetic satellite "ajisai" (egs).
- [16] Kucharski, D., Kirchner, G., Otsubo, T., and Koidl, F., 2015. "A method to calculate zero-signature satellite laser ranging normal points for millimeter geodesy - a case study with ajisai". *Earth Planets and Space*, **67**, 03, p. 34.
- [17] Ariane 40 r/b tracking. <https://www.n2yo.com/satellite/?s=22830>. Accessed: 2020-04-27.